

High Surface Area N-Doped Carbon Fibers with Accessible Reaction Sites for All-Solid-State Lithium-Sulfur Batteries

Xiao Sun, Qiang Li, Daxian Cao, Ying Wang, Alexander Anderson, and Hongli Zhu*

Porous carbon plays a significant role in all-solid-state lithium-sulfur batteries (ASSLSBs) to enhance the electronic conductivity of sulfur. However, the conventional porous carbon used in cell with liquid electrolyte exhibits low efficiency in ASSLSBs because the immobile solid electrolyte (SE) cannot reach sulfur confined in the deep pores. The structure and distribution of pores in carbon highly impact the electrochemical performance of ASSLSBs. Herein, a N-doped carbon fiber with micropores located only at the surface with an ultrahigh surface area of $1519 \text{ m}^2 \text{ g}^{-1}$ is designed. As the porous layer is only on the surface, the sulfur hosted in the pores can effectively contact SE; meanwhile the dense core provides excellent electrical conductivity. Therefore, this structurally designed carbon fiber enhances both electron and ion accessibilities, promotes charge transfer, and thus dramatically improves the reaction kinetic in the ASSLSBs and boosts sulfur utilization. Compared to the vapor grown carbon fibers, the ASSLSBs using PAN-derived porous carbon fibers exhibit three times enhancement in the initial capacity of 1166 mAh g^{-1} at C/20. An exceedingly cycling stability of 710 mAh g^{-1} is maintained after 220 cycles at C/10, and satisfactory rate capability of 889 mAh g^{-1} at C/2 is achieved.

1. Introduction

All-solid-state lithium sulfur batteries (ASSLSBs) have attracted extensive attention because of their remarkable safety and ultrahigh theoretical energy density (2600 Wh kg^{-1}), which is tenfold higher than that of current commercial lithium-ion batteries.^[1] In comparison with Li-S batteries using organic liquid electrolyte, ASSLSBs successfully avoid the active material loss caused by shuttle effects of polysulfides, which can significantly improve cycling stability.^[2] However, the energy densities of current ASSLSBs are still much lower than the theoretical value. The most significant challenge in ASSLSBs is the sluggish charge transfer, including electrons and ions, which can render high overpotential, low voltage efficiency, poor energy efficiency, and low sulfur utilization.^[3,4] More importantly, owing to the huge volume expansion and shrinking of sulfur in the cathode during cycling, the sluggish charge transfer can cause


the pulverization of the electrodes and induce fast capacity decay.^[5] Besides these challenges, point-point contact in solid electrolyte can also render poor lithium-ion transfer both inside the sulfur electrode and at the sulfur/electrolyte interface, representing another main limitation of ASSLSBs.^[6] Therefore, it is crucial to create advanced cathode electrode with improved electron and ion transfer in ASSLSBs.^[2,4]

In liquid cells, the highly porous carbon with a large specific surface area has been widely employed to address the challenges in electrical conductivity, because the porous carbon can provide sufficient reaction sites for sulfur, accommodate the volume change during cycling, and confine the sulfur to address the shuttle effect.^[7,8] Attributed to the excellent flowability and the endowed capillary effects, liquid electrolytes have high accessibility to most sulfur that has been confined in the porous carbon and even the pores buried

deep inside the carbon, which results in high utilization of sulfur. Different from the liquid Li-S batteries that the liquid electrolyte can access pores inside due to its superior mobility and capillary effect, ASSLSBs required more elaborate design of porous carbon structure beyond the high electrical conductivity and high surface area, because SEs can only contact the sulfur located at the outside surface of porous carbon and the sulfur confined deep in the pores inside the carbon is generally inaccessible for SEs. The sulfur hosted in these inaccessible pores is ionically insulated resulting in low reaction kinetic and poor active material utilization. Ideally, in the ASSLSBs, the pores should be located on the surface of the porous carbon to ensure the approachability of the SEs, while the carbon used should also have high electrical conductivity. However, such structural design of porous carbon fiber has not been reported for ASSLSBs yet, though some porous carbons have been used for ASSLSBs.^[5,9]

Traditionally carbon fibers are made from polyacrylonitrile (PAN) polymers through spinning, thermostabilization and carbonization. The PAN-derived porous carbon fibers (PPCF) has high Young's modulus ($230\text{--}588 \text{ GPa}$) and high electrical conductivity ($55\text{--}143 \text{ kS m}^{-1}$).^[10] In this work, based on the PAN carbon fiber, we developed a porous carbon fiber with a core-shell structure and employed it in the ASSLSBs as an electrically conductive additive in the cathode for the first time. A sulfide electrolyte, $\text{Li}_6\text{PS}_5\text{Cl}$, was used because of high ionic conductivity (2 mS cm^{-1}).^[11] The fabricated porous carbon fiber has addressed the abovementioned requirements of carbon for the

X. Sun, Q. Li, D. Cao, Y. Wang, A. Anderson, H. Zhu
Department of Mechanical and Industrial Engineering
Northeastern University
360 Huntington Avenue, Boston, MA 02115, USA
E-mail: h.zhu@neu.edu

 The ORCID identification number(s) for the author(s) of this article can be found under <https://doi.org/10.1002/smll.202105678>.

DOI: 10.1002/smll.202105678

ASSLSBs. Systematical analyses of the fiber morphology, surface area, pore size distribution, and chemical composition of the PPCF revealed that our porous carbon fiber had an ultrahigh-specific surface area after a solid potassium hydroxide (KOH) activation process, which is highly desired in the sulfur cathode to provide enough reaction sites. More importantly, the pores of the PPCF only distributed on the surface after solid-state activation, enabling a good contact with SEs. Besides the high surface area, the one-dimensional (1D) structure of PPCF benefits the building of a low percolation threshold of carbon additives to facilitate electron transfer in the entire electrodes. All these merits of our PPCF make it a highly promising carbon additive for ASSLSBs. Additionally, as compared to a most widely used commercial carbon additive, vapor grown carbon fibers (VGCF), which shows a typical 1D fibrous morphology, our designed porous carbon fiber has exceeded performance. This work sheds light on the development of advanced carbon additives for high-performance ASSLSBs.

2. Results and Discussion

As the only electron conductor in the cathode, carbon additive plays a critical role in determining the electrochemical performance of ASSLSBs. The carbon additive is desired for its large specific surface area on the outside surface to enable sufficient electron accessibility to sulfur and non-block to ion conduction. Here, PPCF and VGCF, which own 1D morphology, were compared. As illustrated in Figure 1a, VGCF exhibited a dense fibrous morphology with limited surface pores resulting in a low specific surface area. The sulfur was mostly in a bulky state

under the limited surface area and no porous confinement in VGCF. When composited with SE in the cathode, the three components (VGCF, sulfur, and SE) were randomly distributed with insufficient contact (Figure 1b). Considering the surface area of VGCF was very low, the contact area between sulfur and VGCF was limited. Therefore, only a tiny fraction of sulfur contacted both the VGCF and SE to be utilized in the electrochemical reaction, which led to a low sulfur utilization and capacity (Figure 1c).

In comparison, the PPCF with high specific surface area and core-shell structure was designed to address the above challenges in VGCF. Figure 1d illustrates the morphology of PPCF-S. The PPCF showed a similar fibrous morphology but with a larger diameter compared to VGCF. More interestingly, the PPCF owned a unique core-shell structure where a porous layer covered the dense core, which contributed to a large outer specific surface area. The surface pores were generated during the solid etching process by solid KOH. After the sulfur infiltration, the PPCF-S maintained its fibrous morphology where the sulfur was confined in the micropores on the porous surface layer. Figure 1e illustrates the distribution of sulfur, PPCF, and SE in the cathode. Attributing to the high surface area, PPCF functioned not only as the electron conductor but also as the host for sulfur. The dense core of PPCF provided fast electron conduction, while the sulfur was confined in the micropores on the surface, avoiding the formation of bulky sulfur. More importantly, this unique structure enabled sulfur to have good contact with both carbon and SEs. As depicted in Figure 1f, the confined sulfur exhibited high electrons and ions accessibility, contributing to remarkable sulfur utilization in the solid-state batteries. The micropores could also alleviate the volume change of sulfur during cycling. All these features enabled PPCF a promising conductive additive for ASSLSBs.

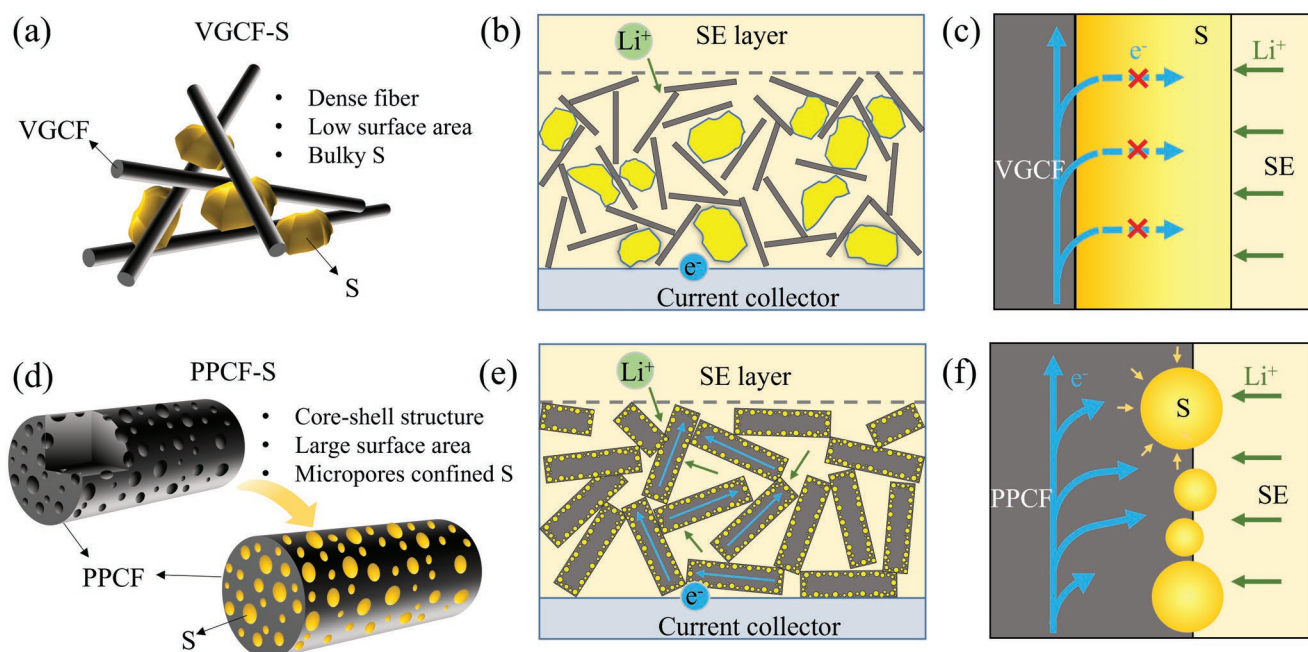


Figure 1. Schematic illustration of the structural effect of carbon additive in the cathode. The morphology of a) VGCF and d) PPCF, and corresponding effects on sulfur deposition. The distributions of sulfur, carbon additive, and SE in the cathodes using b) VGCF and e) PPCF as carbon additives in ASSLSBs, individually. The scenarios that the electrons and ions access to the sulfur in cathodes using c) VGCF and f) PPCF as carbon additives, individually.

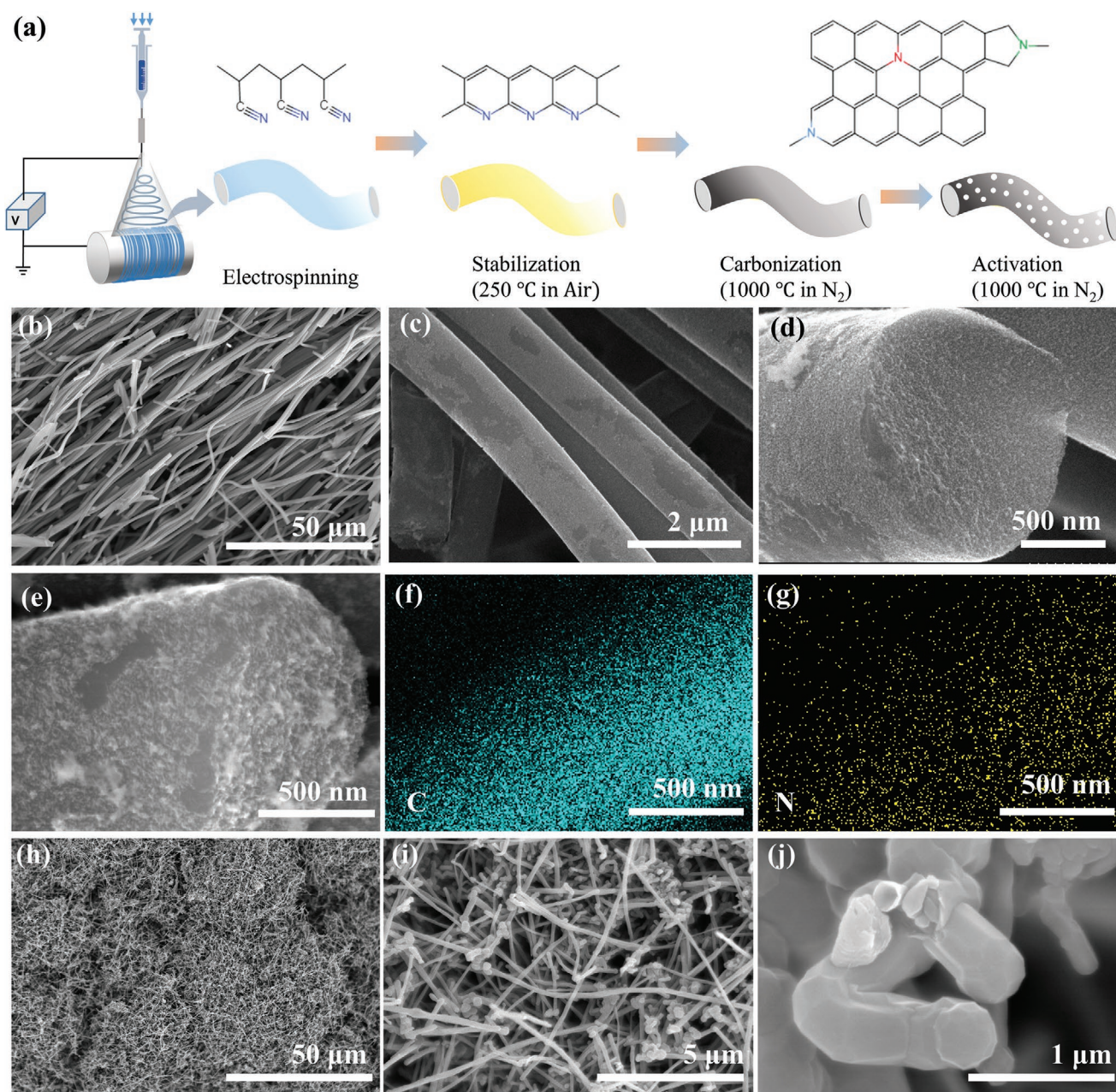


Figure 2. The morphology comparison between PPCF and VGCF. a) The preparation of PPCF through electrospinning, stabilization, carbonization, and activation processes. b–d) SEM images of PPCF under different magnifications to show the core-shell structure. e) SEM image of PPCF and corresponding EDX mapping of f) carbon and g) nitrogen elements. h–j) SEM images of VGCF under different magnification.

The preparation of the porous PPCF fiber was conducted with electrospinning followed by stabilization, carbonization, and activation processes in sequence, as depicted in **Figure 2a**. The PAN powder was dissolved in the *N,N*-dimethylformamide (DMF) to form a 15 wt% solution. When extruded from the needle, the PAN solution droplet experienced electrification and formed a jet.^[12] After stretching and elongation, the fibers were collected on aluminum (Al) foil. Before the carbonization, the as-spun PAN fibers experienced a stabilization process in the air at 250 °C, where the C≡N was converted into C=N (accompanied by the formation of the cyclic structure). After further annealing process in an inert nitrogen (N₂) atmosphere at 1000 °C, the PAN was carbonized into the pre-graphitic carbon

structure to prepare a PAN-derived carbon fiber (PCF). To obtain the porous structure with enlarged surface area, an activation treatment with solid KOH was applied. In this process, the carbon fiber was mixed with KOH powder and then treated at 1000 °C in an inert N₂ atmosphere. The carbon fiber was etched by KOH through the chemical activation, physical activation, and the intercalation of metallic potassium simultaneously (the detailed reaction is listed in Equation (S1)–(S5), Supporting Information).^[13] Because KOH surrounded the surface of the carbon initially, only the surface of the carbon fiber was etched through the solid reaction, and a unique core-shell structure that a porous carbon layer covered on the dense core was successfully prepared.

Scanning electron microscopy (SEM) was employed to investigate the morphology evolution of PPCF. The as-spun PAN showed a fibrous morphology with length in hundreds of micrometers and a diameter of around one micrometer (Figure S1, Supporting Information). After the stabilization, carbonization, and grinding processes, the fiber length of PCF was reduced to $\approx 50 \mu\text{m}$ and the surface was very smooth, demonstrating a nonporous structure (Figure S2, Supporting Information). After the activation process, the PCF turned to be PPCF, the surface of which became coarse and was anchored with abundant nanoparticles (Figure S3, Supporting Information). These particles could be the reaction products of KOH, like K_2O and K_2CO_3 (Equations (S1)–(S5), Supporting Information). After being treated with dialysis, the PPCF exhibited a unique core-shell structure, as shown in Figure 2b–d. The PPCF maintained the 1D fibrous morphology well. The average length was still over $50 \mu\text{m}$, and the diameter did not change (Figure 2b). When further magnified and depicted in Figure 2c, the surface of PPCF was covered by a rough layer and the dense core fiber was observed in some bare regions. Figure 2d shows the cross-section morphology of PPCF, where the dense fiber core was conformally covered by a thin, porous layer. The surface porous layer originated from the activation by KOH. Due to the solid reactions, the porous layer mainly existed on the surface of the carbon (Figure S4, Supporting Information). The dense core fiber could contribute to excellent electron conduction while the porous shell provides enlarged surface area to host sulfur.

In addition, SEM Energy Dispersive X-ray analysis (EDX) elemental mapping of PPCFs (Figure 2e) revealed that there were uniform C (Figure 2f) and N elements (Figure 2g) distribution in PPCFs. The N element arose from the remaining N-containing groups, like pyrrolic N, graphitic N, pyridine N, oxidized N, which were formed in the dehydrogenation process. For comparison, VGCF, which is a commercial carbon additive with a 1D structure, was also investigated as a control sample, as shown in Figure 2h–j. Obviously, the VGCF exhibited a typical fibrous morphology, but the fiber length and diameter were much lower than PPCF. The length was around $10 \mu\text{m}$ and the diameter was 200 nm . In comparison with the straight PPCF, the VGCF tangled with each other. More importantly, the VGCF was a dense fiber with a smooth surface without pores, which has limited surface area.

As aforementioned, carbon additives with a large specific surface area are desired to provide sufficient reaction sites for sulfur. The specific surface area and pore structure of both PPCF and VGCF were investigated by Brunauer–Emmett–Teller (BET) via N_2 adsorption-desorption isotherms. Figure 3a displays the N_2 adsorption/desorption isothermal profiles of PPCF and VGCF. The PPCF possessed an ultrahigh BET specific surface area of $1519 \text{ m}^2 \text{ g}^{-1}$, while the VGCF exhibited much lower value of $191 \text{ m}^2 \text{ g}^{-1}$. The profile of VGCF showed a typical type III shape indicating a nonporous or microporous structure, based on the International Union of Pure and Applied Chemistry (IUPAC) classification.^[14] In contrast, the N_2 adsorption isotherm of PPCF has displayed the type I shape, where the N_2 adsorption mainly happened at the relative pressures lower than 0.1 attributing to the wide presence of micropores ($< 2 \text{ nm}$). No hysteresis cycle was found, further suggesting the PPCF is predominantly populated with

micropores. The pore size distribution of both PPCF and VGCF are compared in Figure 3b. It is evident that the predominant pores exhibited a small size lower than ten angstroms. In comparison, there are only a negligible fraction of pores in VGCF. The numerous micropores explained the ultrahigh-specific area of PPCF in the surface layer that originated from the activation process by solid KOH.

X-ray photoelectron spectra (XPS) was used to compare the chemical structures of PPCF and VGCF. Figure 3c displays the survey spectra of PPCF and VGCF with the characteristic peaks of O 1s and C 1s, with a tiny peak attributed to N 1s observed in PPCF, indicating that N atoms were doped in the PPCF. The N derived from PAN and the content was determined to be 1.27 at%. The high-resolution XPS spectra of C 1s, N 1s, and O 1s of PPCF and VGCF were further analyzed to investigate the bonding configuration. The C 1s spectrum of PPCF was deconvoluted into peaks located at 284.5, 285.9, and 288.9 eV, which can be indexed to C–C, C–N/C–O–C, and C=O, respectively, as depicted in Figure 3d.^[15,16] The main peak located at 284.5 eV demonstrated that there was a large proportion of $\text{sp}^2\text{-C}$, suggesting a high degree of graphitization. The presence of C–O–C and C=O bonds supported the activation process by the KOH as introduced. The high-resolution N 1s spectra shown in Figure 3e reveals that the N atoms in PPCF were in the form of pyrrolic N (399.9 eV), quaternary N (401.0 eV), and oxidized N (402.8 eV).^[15] It has been reported that the quaternary N could enhance the electron conduction and the oxidized N show an excellent catalytic effect on oxygen redox catalysis.^[17] Figure 3f displays the deconvoluted peaks of O 1s located at 531.7, 533.1, and 535.4 eV corresponding to C=O, C–O–C, and H–O–H from adsorbed water, respectively.^[18] For comparison, the surface chemistry of VGCF was also investigated. Figure 3g shows the C 1s spectrum of VGCF where peaks located at 284.4, 285.6, 287.3, and 290.8 eV are attributed to C–C, C–O–C, C=O, and $\pi\text{-}\pi^*$ bonding, respectively.^[19] Moreover, there was no detected signal of N atoms as depicted in Figure 3h, which was the largest difference between VGCF and PPCF in chemical structure. Similarly, the O 1s spectrum of VGCF shown in Figure 3i was deconvoluted into peaks at 531.7, 533.4, and 536.2 eV belonging to the C=O, C–O–C, and H–O–H from adsorbed water, respectively.^[18]

The cathodes using PPCF and VGCF as carbon additives were prepared through a ball milling mixing method followed with an annealing process. Based on the composition, the cathode using PPCF and VGCF as carbon additives were named S-PPCF-SE and S-VGCF-SE. Figure 4a,b compare the SEM images of S-PPCF-SE and S-VGCF-SE cathodes. It is clear that the length of both PPCF and VGCF were reduced to around $5 \mu\text{m}$ after the ball milling process. However, the distribution of sulfur, SE, and carbon additives in these two cathodes are different. In S-PPCF-SE, the PPCF was uniformly dispersed with particles in size of around one micrometer. It was easy to identify these particles. In comparison, the VGCF was embedded into a muddy matrix and no obvious particles were observed. Considering the sulfur was generally in a muddy morphology and SE had its own particle shape, the particles observed in S-PPCF-SE were mainly the SE particles. The muddy matrix in S-VGCF-SE should be the sulfur. Therefore, in S-VGCF-SE, the sulfur was randomly distributed. In contrast, the sulfur

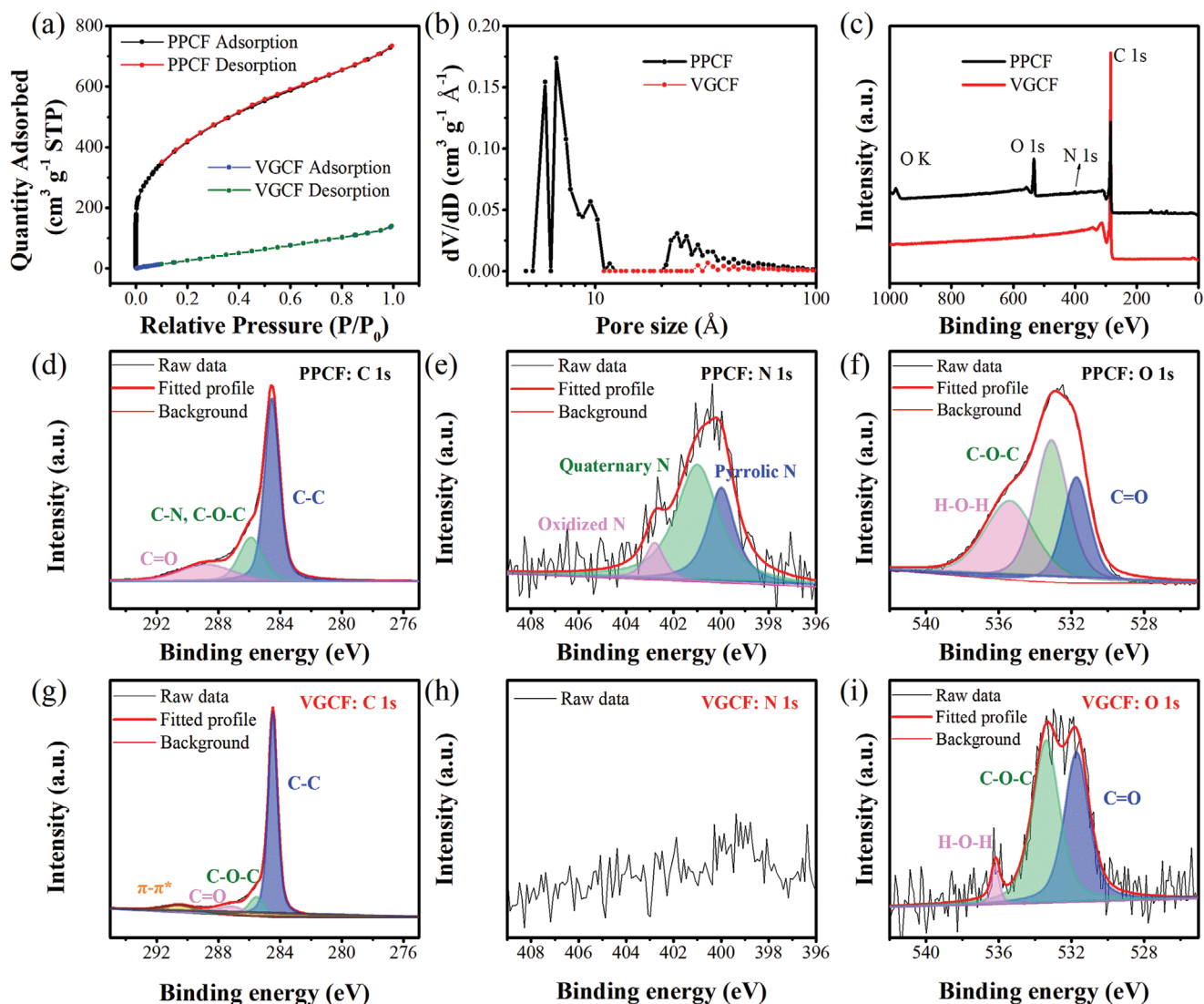


Figure 3. Specific surface area and chemical structure comparisons between PPCF and VGCF. a) N₂ adsorption/desorption isothermal profiles and b) pore size distributions of PPCF and VGCF. c) Survey X-ray photoelectron spectra of both PPCF and VGCF. High-resolution XPS spectra of d) C 1s, e) N 1s and f) O 1s in PPCF, g) C 1s, h) N 1s, and i) O 1s in VGCF.

in S-PPCF-SE was not clearly detected. During the annealing process, the melted sulfur could infiltrate the porous layer on PPCF. Figure S5 (Supporting Information) displays the morphologies of the S-PPCF-SE before annealing. The sample was covered by a muddy matrix which was electron charging suggesting very poor electronic conductivity. These results demonstrated that demonstrates the S was randomly distributed in the sample. In comparison, sulfur can infiltrate the micropores in PPCF during the following annealing process.

Figure 4c shows the X-ray diffraction patterns of PPCF, Li₆PS₅Cl, and S-PPCF-SE before and after annealing. The PPCF showed a broad peak located at 24°. Meanwhile, the Li₆PS₅Cl exhibited a high degree of crystallization, and all the peaks could be indexed to the cubic space groups for argyrodite types, *F*-43m. After the ball milling process, there were some new sharp peaks observed in S-PPCF-SE in comparison with pure Li₆PS₅Cl. These peaks were attributed to the sulfur

(PDF#83-2284),^[20] demonstrating the sulfur was still in the crystalline state. However, after further annealing treatment, the intensity of the peak located at 23° was reduced considerably. This phenomenon also happened in S-VGCF-SE, as depicted in Figure S6 (Supporting Information). This phenomenon was also observed in other porous carbon and explained by the crystalline sulfur was incorporated in the carbon framework after melting infiltration process.^[8]

Raman spectra were utilized to further analyze the S-PPCF-SE, as shown in Figure 4d. Two prominent peaks at 1378 and 1591 cm⁻¹ belonged to the D and G bands of PPCF, respectively.^[21] The D and G bands corresponded to the disordered structures of sp³ carbon and the stretching mode of sp² carbon. The intensity ratio of the D band and G band (*I*_D/*I*_G) was often used to evaluate the crystallization degree of carbon. Here the *I*_D/*I*_G was 0.93 demonstrating the formation of a large proportion of graphitic carbon during the carbonization process.

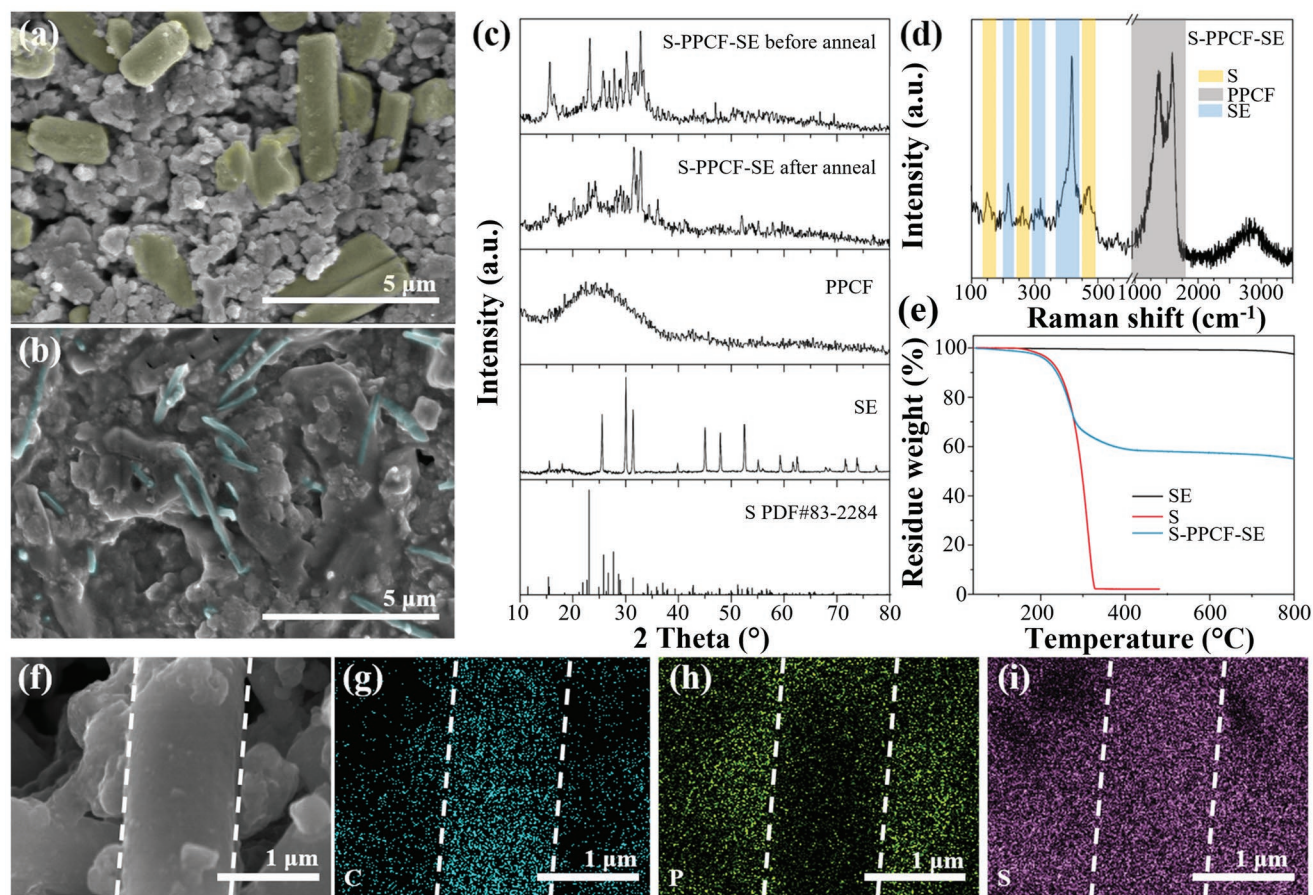


Figure 4. Characterization of cathodes utilizing PPCF and VGCF. SEM images of a) S-PPCF-SE and b) S-VGCF-SE cathodes. c) XRD patterns of S-PPCF-SE before and after annealing, PPCF, $\text{Li}_6\text{PS}_5\text{Cl}$ and sulfur d) Raman spectra of S-PPCF-SE, and e) TGA of S-PPCF-SE, sulfur, and $\text{Li}_6\text{PS}_5\text{Cl}$. f) SEM image and EDX elemental mapping of g) C, h) P, and i) S of the S-PPCF-SE.

Meanwhile, the peaks located at 203, 268, and 428 cm^{-1} belong to the tetrahedra PS_4^{3-} unit in $\text{Li}_6\text{PS}_5\text{Cl}$, while the peaks at 154, 225, and 478 cm^{-1} were attributed to the S–S bond in sulfur.

Figure 4e displays the thermogravimetric analysis (TGA) profiles of S-PPCF-SE, sulfur, and SE to confirm the exact ratio of sulfur in cathode. The $\text{Li}_6\text{PS}_5\text{Cl}$ shows a high stability from room temperature to $800\text{ }^\circ\text{C}$, further confirming the excellent thermal stability of sulfide SE. It is obvious that S-PPCF-SE, and sulfur, showed a huge weight loss at around $300\text{ }^\circ\text{C}$ attributing to the sublimation of sulfur. The sulfur mass loading in S-PPCF-SE is 36%.

The distribution of sulfur in the cathode highly impacted the performance of the entire battery. Figure 4f–i show the SEM images of the PPCF fiber in the S-PPCF-SE and the corresponding EDX element mapping of C, P, and S. Compared with the pristine PPCF, the surface of PPCF in S-PPCF-SE was relatively smooth, explained by the infiltration of sulfur in the porous structure of PPCF. The distribution of sulfur and $\text{Li}_6\text{PS}_5\text{Cl}$ can be distinguished by the element mapping of P. As shown in Figure 4h, there was no P element on the PPCF, but the S element presented, suggesting that the S element on PPCF was derived from the sulfur, not the $\text{Li}_6\text{PS}_5\text{Cl}$. It proved that the sulfur was successfully infiltrated in PPCF. To further prove this conclusion, PPCF and sulfur were directly mixed and

annealed. As displayed in Figure S7 (Supporting Information), there was no aggregation of sulfur observed and the PPCF was clearly distinguished, demonstrating sulfur was all infiltrated in the PPCF.

To evaluate the electrochemical performances of S-PPCF-SE and S-VGCF-SE, ASSLSBs coupling these two cathodes with an In-Li anode was investigated in the voltage range of 0.7–2.7 V (vs. In-Li). Figure 5a displays the galvanostatic charge/discharge profiles of ASSLSBs using S-PPCF-SE, S-PCF-SE, and S-VGCF-SE as cathodes at the current rate of C/20 in the initial cycle. Obviously, as depicted in the inset figure, the S-PCF-SE delivered a negligible capacity of 0.2 mAh g^{-1} , suggesting a poor reaction kinetic and low sulfur utilization. In a significant contrast, S-PPCF-SE showed a high charge (delithiation) capacity of 1061 mAh g^{-1} and discharge (lithiation) capacity of 1166 mAh g^{-1} initially. The greatly enhanced capacity was attributed to the enlarged specific surface area of PPCF. In contrast, S-VGCF-SE delivered a charge capacity of 242 mAh g^{-1} and discharge capacity of 269 mAh g^{-1} , which are dramatically reduced. The unique core-shell structure of PPCF contributes to the higher utilization of sulfur and the enhancement in capacity. In addition, S-PPCF-SE and S-VGCF-SE showed only one pair of discharge/charge plateau demonstrating one-step conversion between sulfur and Li_2S in cycling. This direct conversion

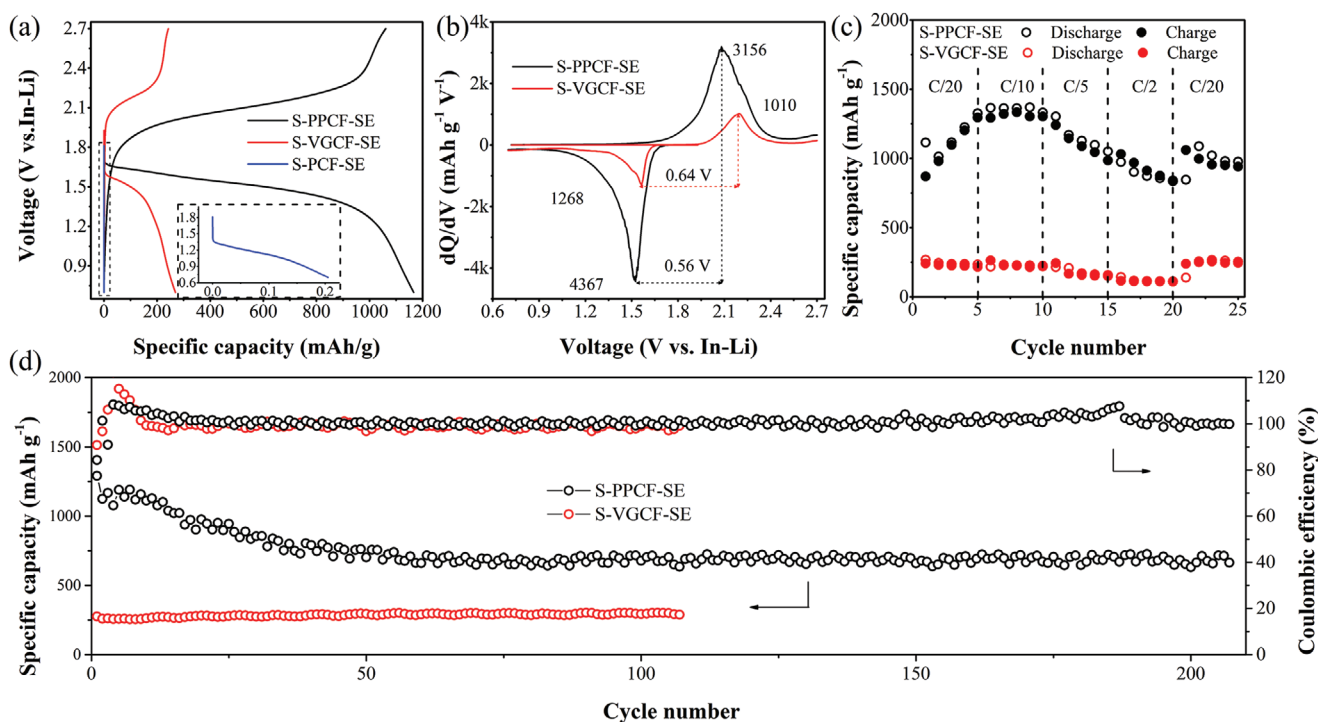


Figure 5. Electrochemical performance evaluation. a) Galvanostatic charge/discharge profiles of ASSLSBs using S-PPCF-SE, S-PCF-SE, and S-VGCF-SE as cathodes at the current rate of C/20. b) Comparison of dQ/dV profiles for the first cycle in ASSLSBs. c) Performances at rates ranging from C/20 to C/2. d) Long-term cycling performance comparison at the rate of C/10. All the cells are tested at room temperature.

(excluding the formation of lithium polysulfides) contributes to the solid reaction.^[22] The potentials in both cells at 50% of the state of charge (SOC) and depth of discharge (DOD) are utilized to evaluate the reaction kinetics. As shown in Figure 5a, the voltage gap of S-VGCF-SE is 748 mV (2.194 V at 50% of SOC and 1.446 V at 50% of DOD). In comparison, the voltage gap of S-PPCF-SE is 599 mV (2.102 V at 50% of SOC and 1.503 V at 50% of DOD), which is 149 mV smaller than S-VGCF-SE. The reduced overpotential explains the faster reaction kinetic and higher voltage efficiency in S-PPCF-SE.

The dramatic capacity difference was highly related to the carbon additives. The differential capacity (dQ/dV) curves of the ASSLSBs in the first cycle were compared in Figure 5b to analyze the reaction kinetic. Both cells displayed only one pair of reduction/oxidation peaks during charge and discharge, aligning with the plateaus in charge/discharge profiles. S-VGCF-SE sample had the reduction/oxidation peaks at 1.56/2.20 V (vs In-Li). In comparison, S-PPCF-SE showed the reduction peak at 1.52 V and the oxidation peak at 2.08 V. The peaks separation between oxidation and reduction onset potential in S-VGCF-SE is 0.64 V and 0.56 V in S-PPCF-SE, demonstrating the S-PPCF-SE owns much faster reaction kinetic. Notably, the S-PPCF-SE showed an anodic peak with a high intensity of 3156 mA h⁻¹ V⁻¹ and a cathodic peak with an intensity of 4367 mA h⁻¹ V⁻¹. In comparison, the S-VGCF-SE shows a weak anodic peak with an intensity of 1010 mA h⁻¹ V⁻¹ and a cathodic peak with an intensity of 1268 mA h⁻¹ V⁻¹. Though the reduction potential is lower, S-PPCF-SE showed an earlier reduction and much larger discharge capacity than those of S-VGCF-SE, demonstrating the utilization of sulfur in the

S-PPCF-SE cathode was much better than S-VGCF-SE. When further oxidized, the S-PPCF-SE showed earlier oxidation and higher capacity than S-VGCF-SE further suggesting enhanced reaction kinetics.

Figure 5c displays the rate performances of the ASSLSBs utilizing PPCF and VGCF as carbon additives, respectively. Obviously, the ASSLSB using PPCF exhibited much higher capacities than the one using VGCF under the same rate. Remarkable rate capacities of 1117, 1364, 1129, and 873 mA h⁻¹ (on average) at current rates of C/20, C/10, C/5, and C/2, respectively. Moreover, the capacity recovered to 1021 mA h⁻¹ when the current rates changed from C/2 to C/20, demonstrating outstanding rate performance. In comparison, the ASSLSB using VGCF delivered a very low capacity of 250 mA h⁻¹ even at a low current rate of C/20. The capacity dropped to 100 mA h⁻¹ when cycled at C/2. The distinctly boosted rate performance was attributed to the enhanced electron and ion accessibilities derived from the unique core-shell structure of PPCF. The sluggish reaction kinetics in ASSLSB using VGCF explained the poor performance.

The cycling performance of S-PPCF-SE and S-VGCF-SE were further investigated in the ASSLSBs measured at C/10, as displayed in Figure 5d. Both cells were activated for three cycles at C/20 before cycling. It is impressive that a high initial charge capacity of 1166 mA h⁻¹ was achieved in S-PPCF-SE, in contrast to the low capacity of 252 mA h⁻¹ in S-VGCF-SE. During cycling, the capacity of S-PPCF-SE gradually decreased to 710 mA h⁻¹ in the initial 50 cycles and then kept stable for over 200 cycles. The initial capacity loss may be attributed to the sulfur in S-PPCF-SE that was dislodged from the PPCF. In

the ball milling and following annealing processes, not all the sulfur was embedded inside the PPCF.

To further investigate the stability of the PPCF, the morphology of S-PPCF-SE after cycling was presented in Figure S8 (Supporting Information). Compared with an electrode prior to cycling, the cycled electrode showed decreased surface roughness and became even denser. It was interesting that the size of the PPCF slightly increased and was surrounded by the amorphous-like matrix. Considering the volume expansion of sulfur during cycling and the pressure generated by the pressurized cell, the structure of PPCF broke to some extent, in agreement with the slow capacity degradation in initial cycles.

3. Conclusion

In summary, an advanced porous carbon fiber, highlighted with a unique core-shell structure, was employed in the cathode of ASSLSBs. With an activation process by solid KOH, an ultrahigh specific surface area of 1519 m² g⁻¹ was obtained, with the pores were mainly located at the outer surface of the fiber. This unique structure promotes the contact of sulfur with both electron conductive carbons and ion conductive SEs, enhancing the charge transfer and electrochemical reaction kinetics. The ultrahigh-specific surface area enabled sufficient area to host sulfur, addressing the low electronic conductivity of sulfur. The confinement of sulfur in the micropores avoided the formation of bulky sulfur and therefore improved sulfur utilization. Meanwhile, the percolation of the 1D fibers accelerated the electron conduction in the entire electrode. All of these merits explain the remarkable rate performances and cycling performance of ASSLSBs utilizing PPCF as carbon additives. Compared with S-VGCF-SE, the S-PPCF-SE showed an overpotential greatly reduced by 149 mV. In the dQ/dV measurement, S-PPCF-SE showed strong anodic and cathodic peaks with high intensity of 3156 and 4367 mAh g⁻¹ V⁻¹ individually which are significantly higher than 1010 and 1268 mAh g⁻¹ V⁻¹ in S-VGCF-SE, demonstrating a greatly improved reaction kinetics. A remarkable rate performance of 889 mAh g⁻¹ at C/2 for S-PPCF-SE was achieved. When cycled at C/10, an exceedingly high capacity of 710 mAh g⁻¹ was maintained after 220 cycles. In comparison, the ASSLSBs using VGCF as carbon additive delivered a low-rate capacity of 100 mAh g⁻¹ at C/2. The structural design in this work will inspire future research for designing porous carbon additives in high energy density ASSLSBs.

Supporting Information

Supporting Information is available from the Wiley Online Library or from the author.

Acknowledgements

X.S., Q.L., and D.C. contributed equally to this work. H.Z. and X.S. acknowledge the financial support from National Science Foundation under Award Number CBET-ES-1924534. The authors thank Dr. Joshua Gallaway in Chemical Engineering at Northeastern University for the sharing of Raman measurement. The authors also acknowledge the

Northeastern University Center for Renewable Energy Technology (NUCRET) for the using of SEM. The authors acknowledge the Kostas Nanomanufacturing Research Center for sharing the XRD. The authors also extend their gratitude to the Center for Nanoscale Systems (CNS) Harvard for providing access to XPS and BET.

Conflict of Interest

The authors declare no conflict of interest.

Data Availability Statement

Research data are not shared.

Keywords

polyacrylonitrile-derived carbon fibers, porous structure, reaction kinetics, solid-state batteries, sulfur cathodes, surface area

Received: September 16, 2021

Revised: October 19, 2021

Published online:

- [1] a) T. Placke, R. Kloepsch, S. Dühnen, M. Winter, *J. Solid State Electrochem.* **2017**, *21*, 1939; b) W. Kang, N. Deng, J. Ju, Q. Li, D. Wu, X. Ma, L. Li, M. Naebe, B. Cheng, *Nanoscale* **2016**, *8*, 16541.
- [2] X. Yang, J. Luo, X. Sun, *Chem. Soc. Rev.* **2020**, *49*, 2140.
- [3] H. Pan, Z. Cheng, P. He, H. Zhou, *Energy Fuels* **2020**, *34*, 11942.
- [4] D. Cao, Y. Zhao, X. Sun, A. Natan, Y. Wang, P. Xiang, W. Wang, H. Zhu, *ACS Energy Lett.* **2020**, *5*, 3468.
- [5] X. Yao, N. Huang, F. Han, Q. Zhang, H. Wan, J. P. Mwiszerwa, C. Wang, X. Xu, *Adv. Energy Mater.* **2017**, *7*, 1602923.
- [6] a) E. Umeshbabu, B. Zheng, Y. Yang, *Electrochem. Energy Rev.* **2019**, *2*, 199; b) C. Yu, S. Ganapathy, E. R. H. v. Eck, H. Wang, S. Basak, Z. Li, M. Wagemaker, *Nat. Commun.* **2017**, *8*, 1086.
- [7] D. Cao, Y. Jiao, Q. Cai, D. Han, Q. Zhang, Y. Ma, A. Dong, H. Zhu, *J. Mater. Chem. A* **2019**, *7*, 3289.
- [8] X. Ji, K. T. Lee, L. F. Nazar, *Nat. Mater.* **2009**, *8*, 500.
- [9] a) T. Kobayashi, Y. Imade, D. Shishihara, K. Homma, M. Nagao, R. Watanabe, T. Yokoi, A. Yamada, R. Kanno, T. Tatsumi, *J. Power Sources* **2008**, *182*, 621; b) L.-P. Hou, H. Yuan, C.-Z. Zhao, L. Xu, G.-L. Zhu, H.-X. Nan, X.-B. Cheng, Q.-B. Liu, C.-X. He, J.-Q. Huang, Q. Zhang, *Energy Storage Mater.* **2020**, *25*, 436; c) S. Kinoshita, K. Okuda, N. Machida, M. Naito, T. Sigematsu, *Solid State Ionics* **2014**, *256*, 97; d) H. Nagata, Y. Chikusa, *J. Power Sources* **2014**, *263*, 141; e) P. Zhu, C. Yan, J. Zhu, J. Zang, Y. Li, H. Jia, X. Dong, Z. Du, C. Zhang, N. Wu, M. Dirican, X. Zhang, *Energy Storage Mater.* **2019**, *17*, 220.
- [10] a) H. Khayyam, R. N. Jazar, S. Nunna, G. Golkarnarenji, K. Badii, S. M. Fakhrhoseini, S. Kumar, M. Naebe, *Prog. Mater. Sci.* **2020**, *107*, 100575; b) B. A. Newcomb, *Composites, Part A* **2016**, *91*, 262.
- [11] D. Cao, Y. Zhang, A. M. Nolan, X. Sun, C. Liu, J. Sheng, Y. Mo, Y. Wang, H. Zhu, *Nano Lett.* **2019**, *20*, 1483.
- [12] J. Xue, T. Wu, Y. Dai, Y. Xia, *Chem. Rev.* **2019**, *119*, 5298.
- [13] J. Wang, S. Kaskel, *J. Mater. Chem.* **2012**, *22*, 23710.
- [14] a) Z. A. ALOthman, *Materials* **2012**, *5*, 2874; b) J. Rouquerol, D. Avnir, C. W. Fairbridge, D. H. Everett, J. M. Haynes, N. Pernicone, J. D. F. Ramsay, K. S. W. Sing, K. K. Unger, *Pure Appl. Chem.* **1994**, *66*, 1739.

- [15] W. He, C. Jiang, J. Wang, L. Lu, *Angew. Chem., Int. Ed.* **2014**, *53*, 9503.
- [16] H. Tang, W. Chen, J. Wang, T. Dugger, L. Cruz, D. Kisailus, *Small* **2018**, *14*, 1703459.
- [17] R. Li, Z. Wei, X. Gou, *ACS Catal.* **2015**, *5*, 4133.
- [18] Y. Yang, X. Sun, Z. Cheng, A. Mukhopadhyay, A. Natan, C. Liu, D. Cao, H. Zhu, *ACS Appl. Energy Mater.* **2020**, *3*, 6249.
- [19] D. W. Porter, M. Orandle, R. R. Mercer, N. Wu, P. Zheng, B. T. Chen, A. Holian, M. Andrew, S. Leonard, M. Wolfarth, S. Friend, L. Battelli, R. F. Hamilton, Y. Hagiwara, T. Koyama, V. Castranova, *NanoImpact* **2017**, *6*, 1.
- [20] M. Chen, Z. Zhang, X. Liu, Y. Li, Y. Wang, H. Fan, X. Liang, Q. Chen, *RSC Adv.* **2020**, *10*, 31773.
- [21] M. Inagaki, Y. Yang, F. Kang, *Adv. Mater.* **2012**, *24*, 2547.
- [22] X. Li, M. Bani, A. Lushington, X. Yang, Q. Sun, Y. Zhao, C. Liu, Q. Li, B. Wang, W. Xiao, C. Wang, M. Li, J. Liang, R. Li, Y. Hu, L. Goncharova, H. Zhang, T.-K. Sham, X. Sun, *Nat. Commun.* **2018**, *9*, 4509.